



Cite this: *J. Mater. Chem. C*, 2022, 10, 13851

Synergistically enhanced electrical transport properties of SrTiO₃ via Fermi level regulation and modulation doping†

Dongmei Li, Dongyang Wang, Xiao Zhang * and Li-Dong Zhao *

SrTiO₃ has gained wide attention as an oxide thermoelectric material due to its high Seebeck coefficient and excellent high-temperature thermal stability. However, its intrinsic insulatory properties hinder its development as a thermoelectric material. Herein, we synergistically improved the electrical transport properties of SrTiO₃ by increasing carrier concentration and maintaining high carrier mobility via Fermi level regulation and modulation doping through co-doping and compositing. Nb and La co-doping notably heightened the carrier concentration and regulated the Fermi level in the conduction band, resulting in an enhanced *ZT* value from that of an insulator in SrTiO₃ to 0.033 in Sr_{0.875}La_{0.125}Ti_{0.85}Nb_{0.15}O₃ at 923 K. The subsequent TiB₂ compositing simultaneously improved carrier concentration ($4.82 \times 10^{17} \text{ cm}^{-3}$) and afforded high carrier mobility ($3.55 \times 10^4 \text{ cm}^2 \text{ V}^{-1} \text{ s}^{-1}$) in the Sr_{0.875}La_{0.125}Ti_{0.85}Nb_{0.15}O₃ + 4% TiB₂ sample at 923 K. The combination of synergistically improved carrier concentration and retained high carrier mobility resulted in an enhanced power factor ($11.04 \mu\text{W cm}^{-1} \text{ K}^{-2}$ at 923 K), maximum *ZT* (0.23 at 923 K) and average *ZT* (0.15 at 473–923 K) in Sr_{0.875}La_{0.125}Ti_{0.85}Nb_{0.15}O₃ + 4% TiB₂ through co-doping and compositing, which matches those of many excellent SrTiO₃-based materials. Our study demonstrated that the thermoelectric properties of SrTiO₃ could be improved via synergistically enhanced electrical transport properties through Fermi level regulation and modulation doping via co-doping and compositing, which will inspire further research on SrTiO₃ and other oxide thermoelectric materials with mediocre electrical transport properties.

Received 21st February 2022,
Accepted 13th March 2022

DOI: 10.1039/d2tc00719c

rsc.li/materials-c

School of Materials Science and Engineering, Beihang University, Beijing 100191, China. E-mail: zhang_xiao@buaa.edu.cn, zhaolidong@buaa.edu.cn

† Electronic supplementary information (ESI) available. See DOI: 10.1039/d2tc00719c



Xiao Zhang

research interests focus on thermoelectric materials and devices as well as thermal barrier coatings.

Dr Xiao Zhang is a postdoctoral research fellow at Beihang University, China. She received her Bachelor of Engineering Degree from the University of Science and Technology, Beijing, in 2013, and received her PhD Degree in Materials Science and Engineering from Beihang University in 2018. She worked at Chongqing University as a faculty staff from 2018 to 2020 before joining Beihang University for postdoctoral research in 2020. Her main

1. Introduction

With the need for green energy, thermoelectric materials have gained growing attention since they can convert heat (industrial waste heat, geothermal heat, etc.) into electricity.¹ The conversion efficiency of thermoelectric materials is determined by *ZT*,

defined as $ZT = \frac{S^2 \sigma}{\kappa} T$, where *S*: Seebeck coefficient, σ : electrical conductivity, and κ : thermal conductivity.^{2–5} Through advanced material design and regulatory strategies, the properties of thermoelectric materials have been rapidly developed in recent decades.^{6,7} However, most traditional thermoelectric materials comprise expensive elements such as Te^{2,8–10} and Ge^{1,11} or toxic elements such as S^{12,13} and Pb.^{14–17} Moreover, the high-temperature resistance and oxidation resistance of traditional thermoelectric materials are mediocre. Therefore, oxide ceramics and oxygenated compounds have been developed for non-toxicity, oxidation resistance, low cost and easy synthesis, satisfying the needs of large-scale production and high-temperature service requirements.^{18,19} Compared with other oxide materials, such as Ca₃Co₃O₉ and NaCo₂O₄, SrTiO₃ (STO) shows superior *S* and excellent thermal stability at high temperatures,^{6,20–22} and its isotropic properties indicate good mechanical properties in

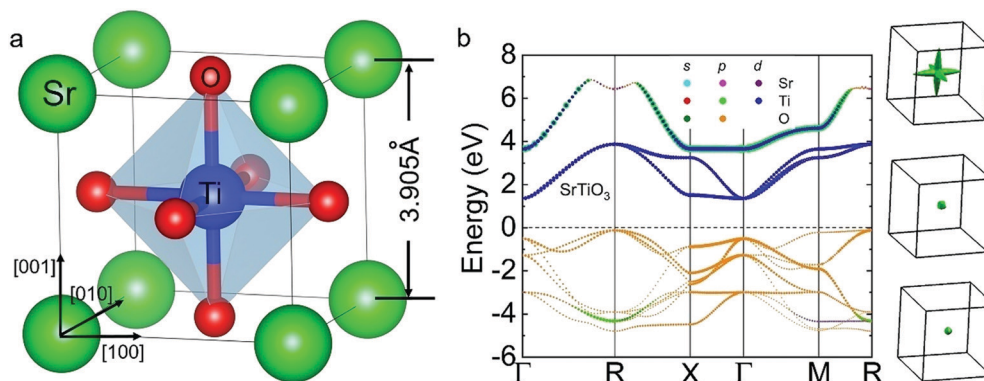


Fig. 1 Structural characterization of SrTiO₃: (a) structure of the crystal and (b) the atomic orbital resolved electronic band structure. The triple degenerate CBM is located at the Γ point. The right panel shows the Fermi energy surface in the first-Brillouin zone with the isosurface level $E_{\text{CBM}} + 0.05$ for these three degenerate bands.

practical applications and a difficulty in fracture in a specific direction, thus gaining more attention as an oxide thermoelectric material.^{23,24}

As shown in Fig. 1(a), SrTiO₃ has a cubic perovskite structure ($Pm\bar{3}m$) and a lattice constant of 3.905 Å at room temperature. The valence band maximum (VBM) and conduction band minimum (CBM) are located at the R and Γ points, respectively, indicating that it is an indirect semiconductor with a large band gap of ~ 1.8 eV (Fig. 1(b)). The VBM mainly originates from the O atom while the CBM mainly results from the Ti-d orbital. Obviously, the CBM is a triple degenerate point and a strong anisotropy of effective mass can be found in the Fermi surface, as shown in the right panel of Fig. 1(b). Additionally, the longitudinal (v_l) and shear (v_s) acoustic velocities, the average sound velocity (v_a) and other elastic properties shown in Table S2 (ESI[†]) correspond to a high κ for the pristine STO material.

The energy band structure calculation results and the sound velocity measurements showed that the pristine STO material as an insulator has ultralow σ and high κ . Roy *et al.*²⁵ reported that the power factor (PF) for Nb-doped SrTiO₃ synthesized by spark plasma sintering (SPS) could reach 33.21 $\mu\text{W cm}^{-1} \text{K}^{-2}$ at 1229 K. Li *et al.*^{26,27} proved that La doping in STO-Nb (Nb-doped SrTiO₃) can not only introduce additional electrons to increase the carrier concentration (n) but also reduce the total energy of the STO-Nb system, effectively increasing the electron-doping efficiency. Besides, Ito *et al.*²⁸ found that TiB₂ could enhance the PF, resulting in a ZT_{max} value of ~ 0.18 for the Sr_{0.95}Y_{0.05}TiO₃ + 5 mass% TiB₂ composite. These motivated us to explore the combined role of co-doping and compositing on the thermoelectric properties of STO.

In this work, we optimized the n of a pristine STO insulator by adjusting the Fermi level (E_F) to enter the conduction band

through Nb-La co-doping. In order to further improve the electrical transport, we composited TiB₂, a high electrical conductivity boride, to introduce modulation doping in the STO matrix, synergistically improving n and maintaining high carrier mobility (μ). Therefore, the PF reached an ideal value in the entire investigated temperature range, with $\sim 11.04 \mu\text{W cm}^{-1} \text{K}^{-2}$ for Sr_{0.875}La_{0.125}Ti_{0.85}Nb_{0.15}O₃ + 4% TiB₂ at 923 K. Owing to the enhanced electrical transport over the broad temperature range, the Sr_{0.875}La_{0.125}Ti_{0.85}Nb_{0.15}O₃ + 4% TiB₂ sample reached a ZT_{max} of ~ 0.23 at 923 K and an average ZT (ZT_{ave}) of ~ 0.15 at 473–923 K, revealing the development potential of SrTiO₃ for high-temperature thermoelectric applications.

2. Results and discussion

As revealed in Fig. 2, the designed improvement strategy for the thermoelectric performance of STO is divided into two consecutive steps: co-doping and compositing. Firstly, STO was transformed from an insulator to a semiconductor by electron-doping: the B-site (Ti⁴⁺) was substituted by Nb⁵⁺ and the A-site (Sr²⁺) was substituted by La³⁺. The experimental results and electronic structure calculations both verify that the La-Nb co-doped STO polycrystal showed measurable σ at room temperature. Secondly, to further synergistically improve n and μ , we composited the optimized La-Nb co-doped STO with TiB₂ with excellent σ . Combining co-doping and compositing, the σ and thermoelectric performance accomplished a striking enhancement in a broad temperature range.

2.1. Transforming STO from an insulator to a semiconductor through increasing carrier concentration via Nb-La co-doping

According to the XRD pattern shown in Fig. 3, the diffraction peaks of all the SrTi_{1-x}Nb_xO₃ ($x = 0.1, 0.125, 0.15, 0.175$)

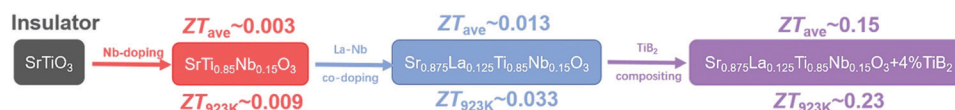


Fig. 2 Roadmap towards the high thermoelectric performance achieved in the SrTiO₃-based samples via co-doping and modulation doping.

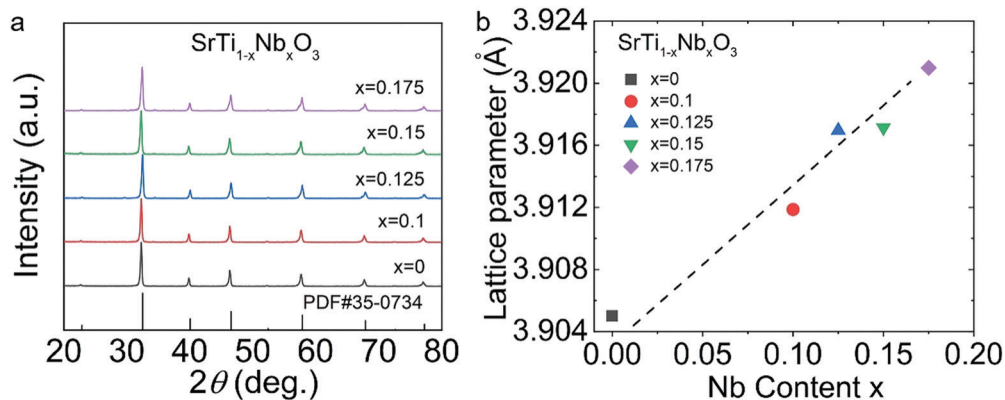


Fig. 3 $\text{SrTi}_{1-x}\text{Nb}_x\text{O}_3$ ($x = 0-0.175$): (a) XRD patterns and (b) lattice constant.

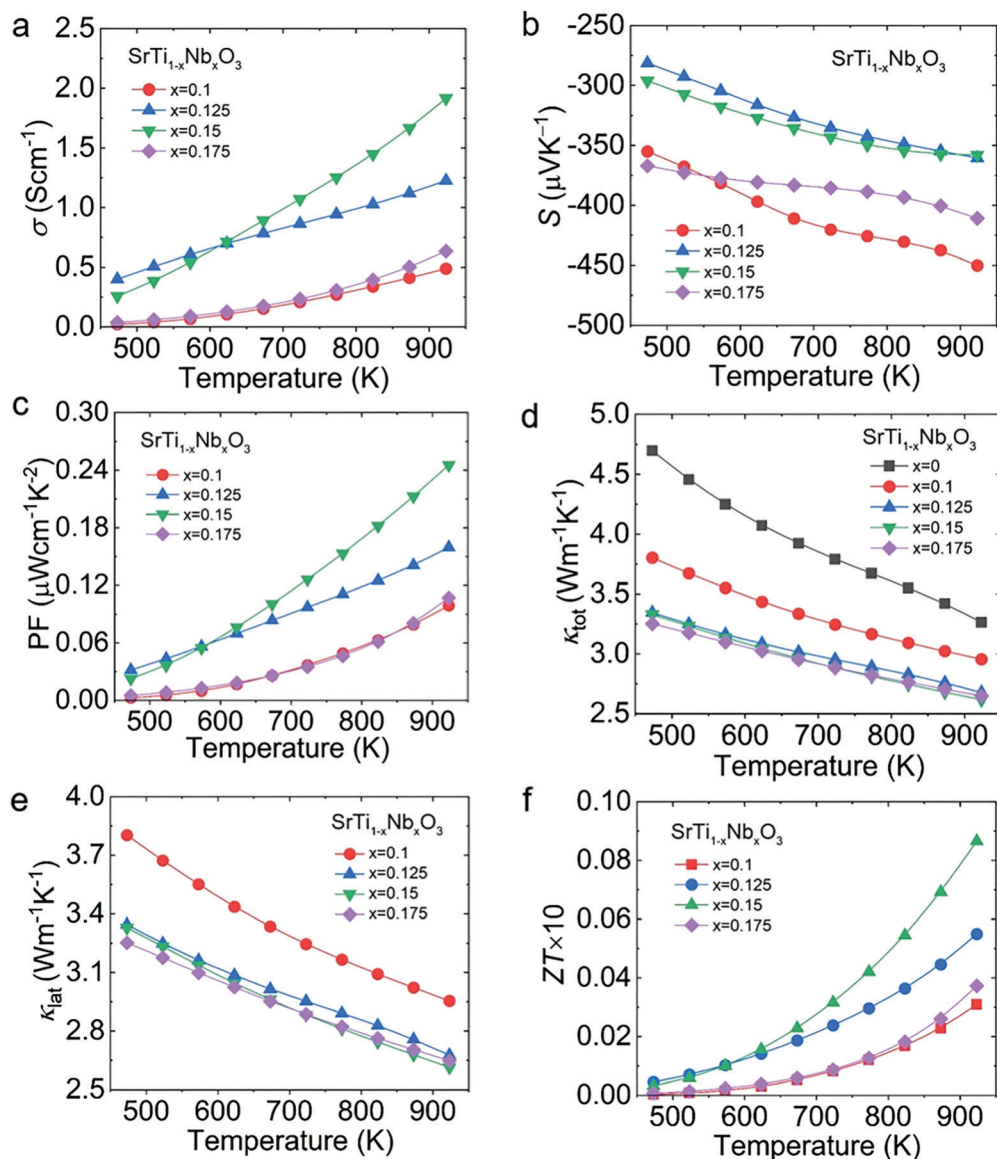


Fig. 4 Thermoelectric performance of $\text{SrTi}_{1-x}\text{Nb}_x\text{O}_3$ ($x = 0-0.175$): (a) σ ; (b) S ; (c) PF; (d) κ_{tot} ; (e) κ_{lat} ; (f) ZT.

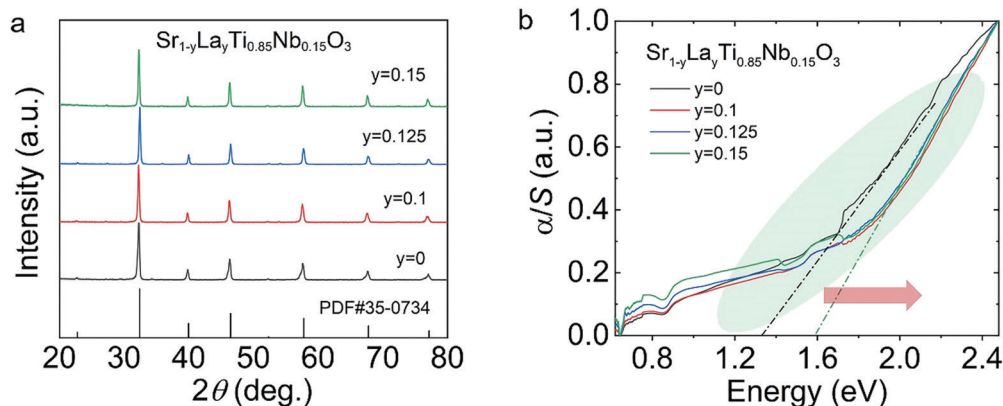


Fig. 5 Structural characterization of $\text{Sr}_{1-y}\text{La}_y\text{Ti}_{0.85}\text{Nb}_{0.15}\text{O}_3$ ($y = 0-0.15$): (a) XRD patterns and (b) absorption coefficient from the Kubelka–Munk method.

samples matched with the standard PDF card (PDF#35-0734) of STO, indicating that STO-based polycrystals were successfully synthesized by the solid-state reaction (SSR) without any impurity phase. Since the ion radius of Nb^{5+} (0.64 Å) is slightly larger than that of Ti^{4+} (0.61 Å), the lattice constants (Fig. 3(b)) increased gradually with increase in doping content.

Fig. 4 displays the thermoelectric properties of $\text{SrTi}_{1-x}\text{Nb}_x\text{O}_3$, revealing the transformation from insulator to semiconductor at 473–923 K with room-temperature insulativity *via* Nb doping. The σ (Fig. 4(a)) of $\text{SrTi}_{1-x}\text{Nb}_x\text{O}_3$ showed a positive correlation with temperature, and generally increased with increasing

doping content. σ reached $\sim 1.9 \text{ S cm}^{-1}$ for the $\text{SrTi}_{0.85}\text{Nb}_{0.15}\text{O}_3$ sample at 923 K. Fig. 4(b) shows that the S values of all samples at 473–923 K are negative, indicating that STO can be transformed from an insulator to an n-type semiconductor *via* electron-doping. The absolute values of all S are greater than $280 \mu\text{V K}^{-1}$, verifying the development potential of STO due to its high $|S|$ in oxide thermoelectric materials.

The decrease of $|S|$ (absolute value of the Seebeck coefficient) and increase of σ are both due to the increased n *via* electron-doping.²⁹ Benefiting from the improved σ , the PF of all samples (Fig. 4(c)) shows enhanced electrical transport properties at high

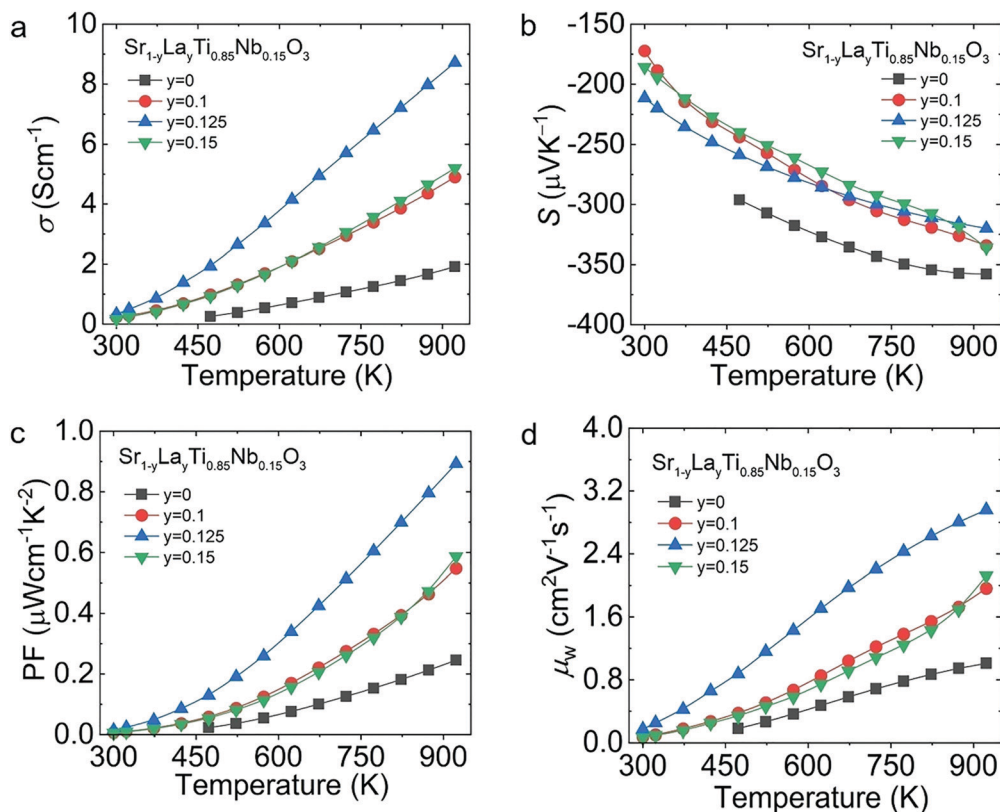


Fig. 6 Electrical transport properties of $\text{Sr}_{1-y}\text{La}_y\text{Ti}_{0.85}\text{Nb}_{0.15}\text{O}_3$ ($y = 0-0.15$): (a) σ ; (b) S ; (c) PF; (d) μ_w .

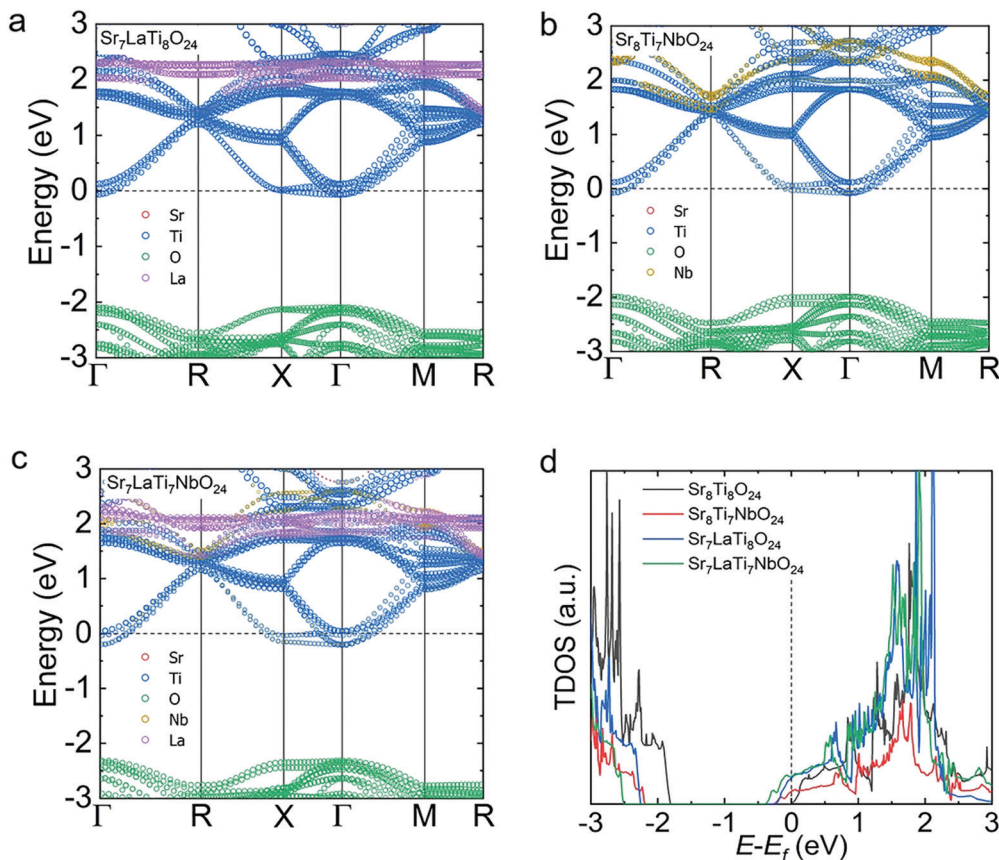


Fig. 7 Electronic band structures and TDOS calculated for the SrTiO₃-based materials: (a) Sr₇LaTi₈O₂₄; (b) Sr₈Ti₇NbO₂₄; (c) Sr₇LaTi₇NbO₂₄; and (d) TDOS near the bottom of the conduction band.

temperatures. The total thermal conductivity (κ_{tot}) (Fig. 4(d)) of the Nb-doped samples is depressed compared with that of un-doped SrTiO₃ due to the enhanced phonon scattering after introducing defects *via* doping.^{30,31} The small difference between κ_{tot} and κ_{lat} seen in Fig. 4(e) indicates that lattice vibration is the main mechanism of heat transfer in the SrTi_{1-x}Nb_xO₃ polycrystal, and that the electrical properties of SrTi_{1-x}Nb_xO₃ are still inferior. Connected with the simultaneously enhanced electrical transport and depressed thermal properties, the ZT_{max} value (Fig. 4(f)) of SrTi_{1-x}Nb_xO₃ ($x = 0.1, 0.125, 0.15, 0.175$) increased from that of an insulator in undoped STO to ~ 0.009 for SrTi_{0.85}Nb_{0.15}O₃ at 923 K, and the ZT_{ave} value (Fig. S2, ESI[†]) was ~ 0.003 for SrTi_{0.85}Nb_{0.15}O₃ at 473–923 K.

Due to the inferior electrical properties and the room-temperature insulativity of SrTi_{1-x}Nb_xO₃, La–Nb co-doping was introduced to further increase the electrical transport properties of SrTi_{0.85}Nb_{0.15}O₃ over a wide temperature range. The XRD patterns of Sr_{1-y}La_yTi_{0.85}Nb_{0.15}O₃ ($y = 0, 0.1, 0.125, 0.15$) in Fig. 5(a) suggest that the La–Nb co-doped STO purity phase was synthesized. The measured band gap of Sr_{1-y}La_yTi_{0.85}Nb_{0.15}O₃ (Fig. 5(b)) showed a slight increase compared with that of SrTi_{0.85}Nb_{0.15}O₃, consistent with the theoretical calculation, which will be discussed later.

The σ of the Sr_{1-y}La_yTi_{0.85}Nb_{0.15}O₃ samples (Fig. 6(a)) increased with temperature, reflecting good semiconductor

behavior and did not reach a peak value within the tested temperature range. Besides, the σ values of Sr_{1-y}La_yTi_{0.85}Nb_{0.15}O₃ are significantly superior to those of SrTi_{0.85}Nb_{0.15}O₃. It is worth noting that the σ of all the La–Nb co-doped samples is measurable at room temperature. All the $|S|$ values indicated that the samples are heavily doped semiconductors, almost linearly proportional to temperature (Fig. 6(b)). Meanwhile, the depressed $|S|$ and enhanced σ for all the La–Nb co-doped samples indicates enhanced n through La and Nb co-doping. Therefore, the PF value (Fig. 6(c)) reached $\sim 0.9 \mu\text{W cm}^{-1} \text{K}^{-2}$ for the Sr_{0.875}La_{0.125}Ti_{0.85}Nb_{0.15}O₃ sample at 923 K. On account of the measured σ and S , we acquired the weighted mobility (μ_{w}) (Fig. 6(d)) of the La–Nb co-doped STO polycrystal. The μ_{w} of Sr_{1-y}La_yTi_{0.85}Nb_{0.15}O₃ increased monotonously with increase in temperature, possibly due to the thermal activation of the grain boundary.^{32,33}

To further understand the doping effect of Nb and La in STO, first-principles calculations were conducted. Compared with the matrix of STO, the introduction of La or Nb can move the E_{F} into the conduction band, mainly due to the additional electrons introduced by Nb and La. As a result, the n obviously improved compared with that of pristine STO. It is worth noting that the E_{F} went further into the conduction band with La–Nb co-doping (Fig. 7(c)), and the band gap increased slightly, in accordance with the measured band gap outcome (Fig. 5(b)).

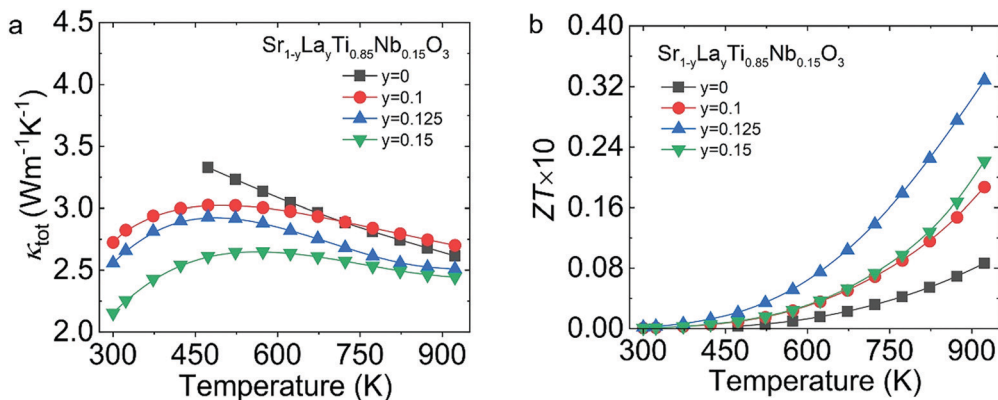


Fig. 8 Thermoelectric transport properties of $\text{Sr}_{1-y}\text{La}_y\text{Ti}_{0.85}\text{Nb}_{0.15}\text{O}_3$ ($y = 0-0.15$): (a) κ_{tot} ; (b) ZT .

Fig. 7(d) shows the corresponding total density of states (TDOS) of $\text{Sr}_8\text{Ti}_8\text{O}_{24}$, $\text{Sr}_7\text{LaTi}_8\text{O}_{24}$, $\text{Sr}_7\text{LaTi}_7\text{NbO}_{24}$ and $\text{Sr}_7\text{LaTi}_7\text{NbO}_{24}$, and a clear entrance of E_F into the conduction band in doped

systems is observed. The TDOS at the E_F is non-zero regardless of La, Nb and La-Nb co-doping, indicating that the doped material has metallic conductivity.

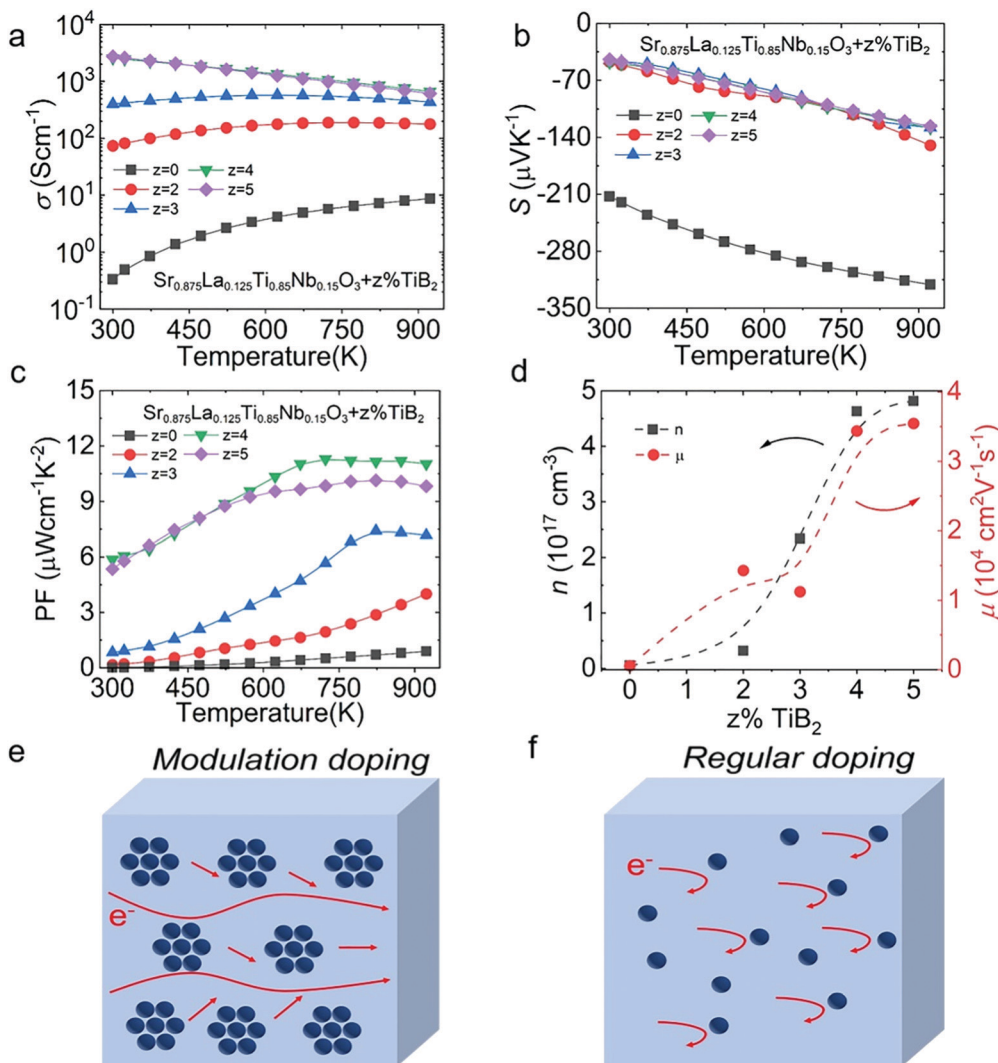


Fig. 9 Electrical transport properties for $\text{Sr}_{0.875}\text{La}_{0.125}\text{Ti}_{0.85}\text{Nb}_{0.15}\text{O}_3 + z\% \text{TiB}_2$ ($z = 0-5$): (a) σ ; (b) S ; (c) PF; (d) n and μ . (e) Modulation-doped semiconductor and (f) regular doped semiconductor.

As displayed in Fig. 8(a), the κ_{tot} for $\text{Sr}_{1-y}\text{La}_y\text{Ti}_{0.85}\text{Nb}_{0.15}\text{O}_3$ showed a negative correlation with La content in the tested temperature range, going from $\sim 3.33 \text{ W m}^{-1} \text{ K}^{-1}$ in $\text{SrTi}_{0.85}\text{Nb}_{0.15}\text{O}_3$ to $\sim 2.61 \text{ W m}^{-1} \text{ K}^{-1}$ of $\text{Sr}_{0.875}\text{La}_{0.125}\text{Ti}_{0.85}\text{Nb}_{0.15}\text{O}_3$ at 473 K. The decreased κ_{tot} is due to the intensive phonon scattering by the point defects due to the mass contrast and lattice local strain introduced by co-doping. Benefiting from the enhanced electrical properties and the weakened thermal transport, the ZT_{max} value reached ~ 0.033 at 923 K (Fig. 8(b)).

2.2. Synergistically enhancing the electrical transport of La-Nb co-doped STO through modulation doping via compositing TiB_2

To further synergistically enhance the n and μ_{W} over the entire tested temperature range, we composited $\text{Sr}_{0.875}\text{La}_{0.125}\text{Ti}_{0.85}\text{Nb}_{0.15}\text{O}_3$ with TiB_2 , which possesses excellent σ ($1 \times 10^5 \text{ S cm}^{-1}$), high melting point (3498 K) and an oxidation resistance temperature in air of 1273 K.^{34,35} This afforded an intermetallic compound with a hexagonal graphite-like two-dimensional network structure, where B and Ti atomic planes appear alternately.³⁶ As depicted in Fig. 9(a), the trend of σ with temperature shows that the semiconductor behavior gradually weakens and the metallic behavior gradually increases with increase in TiB_2 concentration ($z\%$ from 0% to 5%). Particularly, the σ of $\text{Sr}_{0.875}\text{La}_{0.125}\text{Ti}_{0.85}\text{Nb}_{0.15}\text{O}_3$ with 1% and 2% TiB_2 showed monotonic positive correlation with temperature, while the σ of the 3% TiB_2 composite increased first and then decreased, and the electrical properties of the 4% and 5% TiB_2 composites monotonously decreased with increasing

temperature. Additionally, the S (Fig. 9(b)) decreased from $\sim -212 \mu\text{V K}^{-1}$ for $\text{Sr}_{0.875}\text{La}_{0.125}\text{Ti}_{0.85}\text{Nb}_{0.15}\text{O}_3$ to $\sim -48 \mu\text{V K}^{-1}$ for $\text{Sr}_{0.875}\text{La}_{0.125}\text{Ti}_{0.85}\text{Nb}_{0.15}\text{O}_3 + 4\% \text{ TiB}_2$ at room temperature, and from $\sim -321 \mu\text{V K}^{-1}$ for $\text{Sr}_{0.875}\text{La}_{0.125}\text{Ti}_{0.85}\text{Nb}_{0.15}\text{O}_3$ to $\sim 128 \mu\text{V K}^{-1}$ for $\text{Sr}_{0.875}\text{La}_{0.125}\text{Ti}_{0.85}\text{Nb}_{0.15}\text{O}_3 + 4\% \text{ TiB}_2$ at 923 K, indicating the enhancement of electrical transport properties. Therefore, the PF (Fig. 9(c)) of all samples was enhanced over the whole temperature range under investigation, especially for the sample with 4% TiB_2 where it reaches the highest value of $\sim 11 \mu\text{W cm}^{-1} \text{ K}^{-2}$ at $\sim 675 \text{ K}$. Fig. 9(d) shows that the introduction of TiB_2 could effectively increase the n and the μ_{W} , leading to optimization of the σ of STO. The synergistic optimization of the μ_{W} and n may be due to modulation doping. The different carrier transport properties of three-dimensional modulation doping models and ordinary high-density doping are shown in Fig. 9(e and f). In regular doping, the high-density carrier concentration would reduce μ due to the increased ionized impurity scattering. Comparatively, modulation doping is composed of a high-density carrier concentration phase and a low-density carrier concentration phase, which could depress the ionized impurity scattering and enhance μ , synergistically improving n and retaining a high μ . The modulation doping method has already been utilized in many thermoelectric systems, such as SnSe,³⁷ BiCuSeO,³⁸ p-type SiGe,³⁹ P-type ZnSb,⁴⁰ and n-type TeSb.⁴¹

As shown in Fig. 10(a), the electric thermal conductivity (κ_{ele}) of $\text{Sr}_{0.875}\text{La}_{0.125}\text{Ti}_{0.85}\text{Nb}_{0.15}\text{O}_3 + z\% \text{ TiB}_2$ ($z = 0-5$) exhibited a significant increase with increasing TiB_2 content, going from

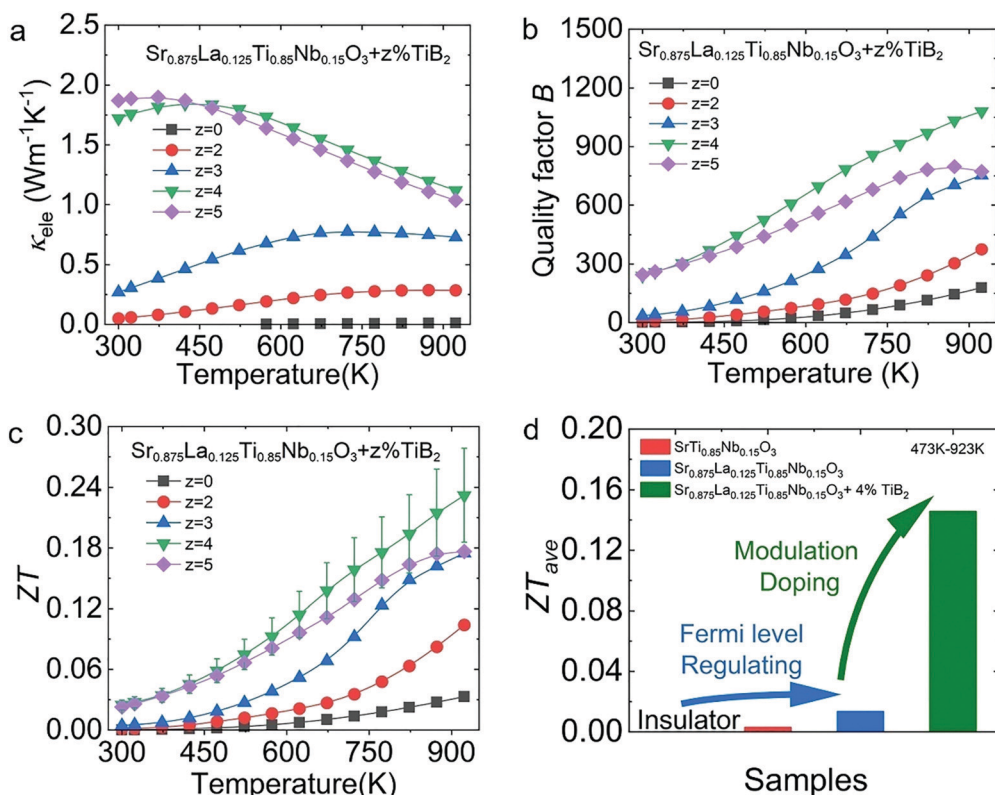


Fig. 10 Thermal transport properties of $\text{Sr}_{0.875}\text{La}_{0.125}\text{Ti}_{0.85}\text{Nb}_{0.15}\text{O}_3 + z\% \text{ TiB}_2$ ($z = 0-5$): (a) σ ; (b) quality factor B ; (c) ZT ; and (d) average ZT of $\text{SrTi}_{0.85}\text{Nb}_{0.15}\text{O}_3$, $\text{Sr}_{0.875}\text{La}_{0.125}\text{Ti}_{0.85}\text{Nb}_{0.15}\text{O}_3$ and $\text{Sr}_{0.875}\text{La}_{0.125}\text{Ti}_{0.85}\text{Nb}_{0.15}\text{O}_3 + 4\% \text{ TiB}_2$.

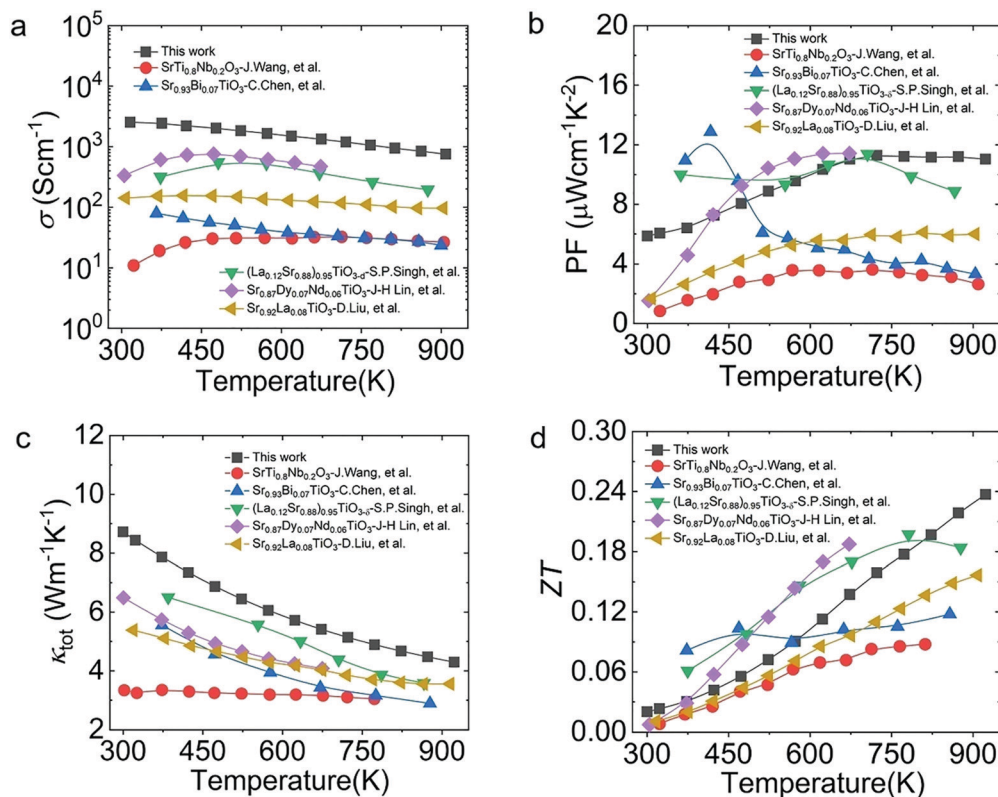


Fig. 11 Thermoelectric properties from this work and from other SrTiO₃-based materials: (a) σ ; (b) PF; (c) κ_{tot} ; (d) ZT .^{31,42–45}

$\sim 0 \text{ W m}^{-1} \text{ K}^{-1}$ in the Sr_{0.875}La_{0.125}Ti_{0.85}Nb_{0.15}O₃ sample to $\sim 1.72 \text{ W m}^{-1} \text{ K}^{-1}$ in the Sr_{0.875}La_{0.125}Ti_{0.85}Nb_{0.15}O₃ + 4% TiB₂ sample at 300 K. According to Fig. 10(b), the heightened electrical transport properties through modulation doping boost the quality factor (B) of these samples in the tested temperature range. Therefore, the sample with 4% TiB₂ obtained a ZT_{max} value of ~ 0.23 at 923 K (Fig. 10(c)), and TiB₂ improved the thermoelectric performance of the STO-based materials over the complete tested temperature range. The optimal performance of the Nb-doped, La–Nb co-doped and modulation-doped samples, with ZT_{ave} values of ~ 0.003 , ~ 0.013 , and ~ 0.15 at 473–923 K, respectively (Fig. 10(d)), showed the significant benefits of the synergetic improvement of n and μ .

We compared the thermoelectric performance of the materials in this work with that of other reported work on STO systems, including SrTi_{0.8}Nb_{0.2}O₃,³¹ Sr_{0.93}Bi_{0.07}TiO₃,⁴² (La_{0.12}Sr_{0.88})_{0.95}TiO_{3– δ} ,⁴³ Sr_{0.87}Dy_{0.07}Nd_{0.06}TiO₃⁴⁴ and Sr_{0.92}La_{0.08}TiO₃,⁴⁵ as shown in Fig. 11. Due to the significantly heightened σ and PF values over the whole tested temperature range, the ZT_{max} of our work showed strong competitiveness among the STO systems, indicating that STO has the potential to become an excellent thermoelectric material.

3. Conclusion

In this study, the thermoelectric properties of SrTiO₃ were gradually enhanced by synergistically improving electrical

transport by increasing n and retaining high μ via E_{F} regulation and modulation doping through co-doping and compositing. Firstly, we introduced Nb doping to adjust the E_{F} of the pristine STO material to enter the conduction band, transforming it from an insulator to a semiconductor. Secondly, the La–Nb co-doped samples showed obvious semiconductor behavior even at 300 K due to the enhanced n . Thirdly, TiB₂ compositing simultaneously improved the n with high μ in SrTiO₃ through modulation doping. Therefore, a promising new kind of n-type STO-based polycrystal was obtained through co-doping and compositing, and the ZT_{max} value of Sr_{0.875}La_{0.125}Ti_{0.85}Nb_{0.15}O₃ + 4% TiB₂ reached ~ 0.23 at 923 K, with a $ZT_{\text{ave}} \sim 0.15$ at 473–923 K. Despite the advancements mentioned above, there is still potential for future research progress, such as reducing thermal conductivity through enhanced phonon scattering.

Conflicts of interest

There are no conflicts of interest to declare.

Acknowledgements

This work was supported by the National Key Research and Development Program of China (2018YFA0702100 and 2018YFB0703600), National Natural Science Foundation of China (52002042), the National Science Fund for Distinguished Young Scholars (51925101), China Postdoctoral Science Foundation

(2021M690280), Natural Science Foundation of Chongqing, China, cstc2019jcyj-msxmX0554, National Postdoctoral Program for Innovative Talents (BX20200028), and the high performance computing (HPC) resources at Beihang University.

References

- 1 R. Basu and A. Singh, *Mater. Today Phys.*, 2021, **21**, 100468.
- 2 G. Tan, W. G. Zeier, F. Shi, P. Wang and M. G. Kanatzidis, *Chem. Mater.*, 2015, **27**, 7801–7811.
- 3 Z. G. Chen, X. Shi, L. D. Zhao and J. Zou, *Prog. Mater. Sci.*, 2018, **97**, 283–346.
- 4 X. Y. Liu, D. Y. Wang, H. J. Wu, J. F. Wang, Y. Zhang, G. T. Wang, S. J. Pennycook and L. D. Zhao, *Adv. Funct. Mater.*, 2019, **29**, 1806558.
- 5 C. Chang, G. J. Tan, J. Q. He, M. G. Kanatzidis and L. D. Zhao, *Chem. Mater.*, 2018, **30**, 7355–7367.
- 6 X. L. Shi, H. Wu, Q. Liu, W. Zhou and Z. G. Chen, *Nano Energy*, 2020, **78**, 105195.
- 7 C. Chang, D. Y. Wang, D. S. He, W. K. He, F. Y. Zhu, G. T. Wang, J. Q. He and L. D. Zhao, *Adv. Energy Mater.*, 2019, **9**, 1901334.
- 8 B. C. Qin, Y. Xiao, Y. M. Zhou and L. D. Zhao, *Rare Met.*, 2018, **37**, 343–350.
- 9 Y. Xiao, D. Y. Wang, B. C. Qin, J. F. Wang, G. T. Wang and L. D. Zhao, *J. Am. Chem. Soc.*, 2018, **140**, 13097–13102.
- 10 D. Wu, Y. L. Pei, Z. Wang, H. Wu, L. Huang, L. D. Zhao and J. He, *Adv. Funct. Mater.*, 2014, **24**, 7763–7771.
- 11 Y. T. Qiu, Y. Jin, D. Y. Wang, M. J. Guan, W. K. He, S. Peng, R. H. Liu, X. Gao and L. D. Zhao, *J. Mater. Chem. A*, 2019, **7**, 26393–26401.
- 12 W. K. He, D. Y. Wang, J. F. Dong, Y. Qiu, L. W. Fu, Y. Feng, Y. J. Hao, G. T. Wang, J. F. Wang, C. Liu, J. F. Li, J. Q. He and L. D. Zhao, *J. Mater. Chem. A*, 2018, **6**, 10048–10056.
- 13 Y. L. Pei, H. Wu, J. Sui, L. Jing, D. Berardan, C. Barreateau, P. Lin, N. Dragoe, W. S. Liu and J. He, *Energy Environ. Sci.*, 2013, **6**, 1750–1755.
- 14 M. Orihashi, Y. Noda, H. T. Kaibe and I. A. Nishida, *Mater. Trans.*, 2007, **39**, 672–678.
- 15 M. A. Ali, S. A. Dar, A. A. AlObaid, T. I. Al-Muhimeed, H. H. Hegazy, G. Nazir and G. Murtaza, *J. Phys. Chem. Solids*, 2021, **159**, 110258.
- 16 E. J. Skoug, J. D. Cain and D. T. Morelli, *J. Alloys Compd.*, 2012, **506**, 18–21.
- 17 X. Qian, H. J. Wu, D. Y. Wang, Y. Zhang, J. F. Wang, G. T. Wang, L. Zheng, S. J. Pennycook and L. D. Zhao, *Energy Environ. Sci.*, 2019, **12**, 1969–1978.
- 18 X. X. Zhang, C. Chang, Y. Zhou and L. D. Zhao, *Materials*, 2017, **10**, 198.
- 19 W. W. Qu, X. X. Zhang, B. F. Yuan and L. D. Zhao, *Rare Met.*, 2018, **37**, 79–94.
- 20 N. M. Ferreira, N. R. Neves, M. C. Ferro, M. A. Torres and A. V. Kovalevsky, *J. Eur. Ceram. Soc.*, 2019, **39**, 4184–4188.
- 21 C. A. Qi, C. Hnz, B. Yz, A. Hm, C. Xcw and A. Xj, *Ceram. Int.*, 2022, **48**, 9014–9023.
- 22 Y. Kodama, N. Murayama and Y. T. Yasukawa, *J. Mater. Sci. Lett.*, 1998, **17**, 1999–2001.
- 23 M. A. Carpenter, C. J. Howard, K. S. Knight and Z. Zhang, *J. Phys.*, 2006, **18**, 10725–10749.
- 24 M. Guennou, P. Bouvier, J. Kreisel and D. Machon, *Phys. Rev. B: Condens. Matter Mater. Phys.*, 2010, **81**, 054115.
- 25 P. Roy, V. Pal and T. Maiti, *Ceram. Int.*, 2017, **43**, 12809–12813.
- 26 Y. Miao, L. Liu, C. Y. Fang, C. Qiqige and A. Wang, *J. Alloys Compd.*, 2016, **665**, 7–12.
- 27 J. Wang, B. Y. Zhang, H. J. Kang, L. Yan and L. D. Zhao, *Nano Energy*, 2017, **35**, 387–395.
- 28 O. Naoto and I. Mikio, *Composites, Part B*, 2016, **88B**, 108–113.
- 29 H. Muta, K. Kurosaki and S. Yamanaka, *J. Alloys Compd.*, 2003, **350**, 292–295.
- 30 N. Wang, H. Chen, H. He, W. Norimatsu, M. Kusunoki and K. Koumoto, *Sci. Rep.*, 2013, **3**, 3449.
- 31 J. Wang, X. X. Ye, X. B. Yaer, B. Y. Zhang, W. Ma and L. Miao, *Scr. Mater.*, 2015, **99**, 25–28.
- 32 W. K. He, B. C. Qin and L. D. Zhao, *Chin. Phys.*, 2020, **37**, 087104.
- 33 G. J. Snyder, A. H. Snyder, M. Wood, R. Gurunathan, B. H. Snyder and C. Niu, *Adv. Mater.*, 2020, **32**, 2001537.
- 34 X. Zhang, Z. Zhang, W. Wang, J. Shan, H. Che, J. Mu and G. Wang, *J. Am. Ceram. Soc.*, 2017, **100**, 3099–3107.
- 35 S. Song, T. Zhang, C. Xie, J. Zhou, R. Li and Q. Zhen, *J. Am. Ceram. Soc.*, 2020, **103**, 719–723.
- 36 O. Popov, T. Avramenko and V. Vishnyakov, *Mater. Today Commun.*, 2020, **26**, 101756.
- 37 L. D. Zhao, S. H. Lo, Y. Zhang, H. Sun, G. Tan, C. Uher, C. Wolverton, V. P. Dravid and M. G. Kanatzidis, *Nature*, 2014, **508**, 373–377.
- 38 Y. L. Pei, H. Wu, D. Wu, F. Zheng and J. He, *J. Am. Chem. Soc.*, 2014, **136**, 13902–13908.
- 39 B. Yu, M. Zebarjadi, H. Wang, K. Lukas, H. Wang, D. Wang, C. Opeil, M. Dresselhaus, G. Chen and Z. Ren, *Nano Lett.*, 2012, **12**, 2077–2082.
- 40 M. Amsler, S. Goedecker, W. G. Zeier, G. J. Snyder, C. Wolverton and L. Chaput, *Chem. Mater.*, 2016, **28**, 2912–2920.
- 41 M. Koirala, H. Zhao, M. Pokharel, S. Chen and T. Dahal, *Appl. Phys. Lett.*, 2013, **102**, 213111.
- 42 C. Cong, A. Mb, A. Fg and A. Fd, *J. Materiomics*, 2019, **5**, 88–93.
- 43 S. P. Singh, N. Kanas, T. D. Desissa, M. Johnsson and K. Wiik, *J. Eur. Ceram. Soc.*, 2019, **40**, 401–407.
- 44 J. H. Lin, C. S. Hwang and F. R. Sie, *Mater. Res. Bull.*, 2020, **122**, 110650.110651–110650.110658.
- 45 D. Liu, Y. Zhang, H. Kang, J. Li, Z. Chen and T. Wang, *J. Eur. Ceram. Soc.*, 2018, **38**, 807–811.